INTERNATIONAL JOURNAL FOR NUMERICAL AND ANALYTICAL METHODS IN GEOMECHANICS
Int. J. Numer. Anal. Meth. Geomech. 2013; **37**:2916–2936
Published online 11 February 2013 in Wiley Online Library (wileyonlinelibrary.com). DOI: 10.1002/nag.2168

A fracture mapping and extended finite element scheme for coupled deformation and fluid flow in fractured porous media

Anthony R. Lamb[1,*,†], Gerard J. Gorman[1] and Derek Elsworth[2]

[1]*Department of Earth Science and Engineering, Imperial College London, South Kensington Campus, London, SW7 2AZ, U.K.*
[2]*Department of Energy and Mineral Engineering and Centre for Geomechanics, Geofluids, and Geohazards (G3), Pennsylvania State University, University Park, Pennsylvania, U.S.A.*

SUMMARY

This paper presents a fracture mapping (FM) approach combined with the extended finite element method (XFEM) to simulate coupled deformation and fluid flow in fractured porous media. Specifically, the method accurately represents the impact of discrete fractures on flow and deformation, although the individual fractures are not part of the finite element mesh. A key feature of FM-XFEM is its ability to model discontinuities in the domain independently of the computational mesh. The proposed FM approach is a continuum-based approach that is used to model the flow interaction between the porous matrix and existing fractures via a transfer function. Fracture geometry is defined using the level set method. Therefore, in contrast to the discrete fracture flow model, the fracture representation is not meshed along with the computational domain. Consequently, the method is able to determine the influence of fractures on fluid flow within a fractured domain without the complexity of meshing the fractures within the domain. The XFEM component of the scheme addresses the discontinuous displacement field within elements that are intersected by existing fractures. In XFEM, enrichment functions are added to the standard finite element approximation to adequately resolve discontinuous fields within the simulation domain. Numerical tests illustrate the ability of the method to adequately describe the displacement and fluid pressure fields within a fractured domain at significantly less computational expense than explicitly resolving the fracture within the finite element mesh. Copyright © 2013 John Wiley & Sons, Ltd.

Received 20 February 2012; Revised 25 October 2012; Accepted 13 December 2012

KEY WORDS: coupled model; porous media; extended finite element method; fractured media; continuum model

1. INTRODUCTION

Deformation coupled with fluid flow in porous media is an important process in areas such as groundwater hydrology, reservoir engineering and CO_2 storage [1]. Coupled deformation and fluid flow reservoir simulations are conducted in stress sensitive, naturally fractured hydrocarbon reservoirs to accurately capture changes in stress-dependent permeabilities that may occur during production as the fluid pressure varies with time. Although not all hydrocarbon reservoirs are located in geologically naturally fractured reservoirs, coupled simulation still plays an important role because compactive and shear deformations may still exert an important influence on reservoir production [2]. Modelling coupled fluid flow and deformation within reservoirs is necessary for predicting the impact of subsidence of production and well failures, guiding well placement and avoiding ground subsidence or heave.

*Correspondence to: Anthony R. Lamb, Department of Earth Science and Engineering, Imperial College London, South Kensington Campus, London, SW7 2AZ, U.K.
†E-mail: a.lamb07@imperial.ac.uk

The mechanics of the coupled behaviour within porous media was initially formulated by Biot [3]. Biot's formulation treats the material skeleton as a single porosity/permeability poroelastic solid and couples its deformation to the laminar flow of the pore fluid through compressibility and continuity. Despite the effectiveness of this coupled formulation for porous media, it is not adequate when dealing with fractured porous media that are composed of discrete fractions of differing solid compressibilities and permeabilities [4, 5]. Barenblatt *et al*. [6] introduced the dual continuum concept by modelling flow through a non-deformable, fractured porous medium. The dual continuum concept provides a mathematical framework for the fluid flow interaction between the matrix domain and fractures and was originally applied to the field of reservoir engineering by Warren and Root [7] to characterize naturally fractured reservoirs.

The dual continuum concept is subdivided into the dual porosity and dual permeability approaches. The dual porosity approach assumes that the porous matrix is discontinuous and flow within the domain is achieved via the fractured network. The simulated fluid flow is directly affected by fracture network connectivity and distribution. In contrast, the dual permeability model assumes that the matrix is continuous and fluid flow occurs within both the matrix and fractures. Fracture network connectivity is not required when using the dual permeability method.

An alternative to the dual continuum approach that has received considerable interest over the last few years in the field of reservoir simulation and hydrology is the discrete fracture flow model approach [8–11]. Fractures are represented within the domain in a spatially explicit manner and are discretized along with the matrix domain. Although this approach considers the real fracture geometry and orientation, the method is computationally expensive, and the meshes can be challenging and time consuming to generate. Therefore, its use is restricted to domains with low fracture density.

The fracture mapping (FM) approach presented combines the merits of both the discrete and continuum approaches; fracture geometry is preserved without having to mesh existing fractures within the simulation domain. Elements intersected by a fracture are treated as two overlapping elements, a matrix element and a fracture element. The orientation and permeability of the fracture are then mapped to the fracture element. The approach adopts the transfer function presented by Barenblatt *et al*. [6] to account for fluid flow interaction between the overlapping matrix and fracture elements. Individual fractures are incorporated into the simulation domain by using the level set method (LSM) introduced by Osher and Sethian [12]. LSM provides a mathematical description of fractures within the domain rather than an explicit representation of the crack geometry. The method represents an interface, in this case a fracture, as the zero of a function called the level set function [13].

A finite element continuum approach can be used to describe the coupled deformation and fluid flow within a fractured porous medium [14, 15]; however, without modification, this method is unable to address the discontinuity that exists in the displacement field across fractures within the domain [16–18]. The FM method is therefore combined with extended finite element method (XFEM) to capture the effect that deformation across fractures may have on the fluid flow within a domain. The FM-XFEM formulation presented assumes that the geometry of fractures within the domain remains constant, that is, fracture length and width remains the same during numerical simulations. Unlike the standard finite element method, XFEM can be used to model discontinuities independently of the mesh. The method has gained much attention in recent years because of its accuracy and versatility in simulating discontinuities [19–28].

The remainder of this paper is outlined as follows. The next section covers the governing equations that describe coupled deformation and fluid flow in porous media. The FM that is used to capture the flow interaction between the porous matrix and fracture is then described. General concepts of XFEM and the element decomposition required for numerical integration are briefly recalled followed by the discretized form of the coupled deformation and fluid flow governing equations. Finally, numerical simulations are performed on a two-dimensional (2D) plane strain example and the results discussed.

2. GOVERNING EQUATIONS

Biot's theory [3] describes the physical process of elastic deformation and fluid flow in porous media. The stress and strain matrices take the following forms in 2D by using Voigt notation:

DOI: 10.1002/nag

$$\boldsymbol{\sigma} = \left[\sigma_x, \sigma_y, \tau_{xy}\right]^{\mathrm{T}}, \tag{1}$$
$$\boldsymbol{\varepsilon} = \left[\varepsilon_x, \varepsilon_y, \gamma_{xy}\right]^{\mathrm{T}},$$

where σ_x, σ_y and τ_{xy} represent the stress in the x and y directions and shear stress, respectively, and ε_x, ε_y and γ_{xy} represent the strain in the x and y directions and shear strain, respectively. A saturated soil/rock mass can be viewed as a two-phase deformable porous medium in which the pores are filled with a liquid.

Biot's theory defines the force equilibrium of the soil–water mixture:

$$\nabla_s^{\mathrm{T}}\boldsymbol{\sigma} + \rho\mathbf{g} = 0, \tag{2}$$

where $\boldsymbol{\sigma}$ is total stress tensor, $\mathbf{g}$ is gravity, ρ is the averaged density of a multiphase system and ∇_s is the symmetric gradient operator matrix given by

$$\nabla_s = \begin{bmatrix} \partial/\partial x & 0 \\ 0 & \partial/\partial y \\ \partial/\partial y & \partial/\partial x \end{bmatrix}. \tag{3}$$

The total stress of the system, assuming that tension is positive, is given by

$$\boldsymbol{\sigma} = \boldsymbol{\sigma}'' - \bar{\alpha}\mathbf{m}P_w, \tag{4}$$

where $\boldsymbol{\sigma}''$ is a general form of the effective stress, P_w is the water pore pressure in the porous matrix, $\mathbf{m} = [110]^{\mathrm{T}}$ in two dimensions and $\bar{\alpha}$ is the Biot's compressibility coefficient that is defined by

$$\bar{\alpha} = 1 - \frac{K_T}{K_s}, \tag{5}$$

where K_T is the bulk modulus of the skeleton and K_s is the bulk modulus of the grain material. Equation (5) represents Terzaghi's effective stress principle that has been modified to take into account the compressibility of the system through the inclusion of Biot's compressibility coefficient.

The constitutive stress–strain relationship of the solid phase is given by

$$d\boldsymbol{\sigma}'' = \mathbf{D}d\boldsymbol{\varepsilon}, \tag{6}$$

in which $\mathbf{D}$ is the linear elastic material matrix and $\boldsymbol{\varepsilon}$ is the strain of the system. For 2D plane stress problems, $\mathbf{D}$ is defined as

$$\mathbf{D} = \frac{E}{1-v^2}\begin{bmatrix} 1 & v & 0 \\ v & 1 & 0 \\ 0 & 0 & \dfrac{1-v}{2} \end{bmatrix}, \tag{7}$$

and for plane strain, it is defined as:

$$\mathbf{D} = \frac{E}{(1+v)(1-2v)}\begin{bmatrix} 1-v & v & 0 \\ v & 1-v & 0 \\ 0 & 0 & \dfrac{1}{2}-v \end{bmatrix}, \tag{8}$$

where E is the modulus of elasticity and v is Poisson's ratio.

The relationship between the change in strain, $d\boldsymbol{\varepsilon}$, and the change in displacement, $d\mathbf{u}$, is given by

$$d\boldsymbol{\varepsilon} = \nabla_s d\mathbf{u}. \tag{9}$$

DOI: 10.1002/nag

This linear relationship is only valid under the assumption of small strain theory where the components of $\nabla_s \mathbf{u}$ are much smaller in magnitude than 1.

Darcy's seepage velocity is given by

$$v_d = \frac{\mathbf{K}_m}{\mu_w}(-\nabla P_w + \rho \mathbf{g}). \tag{10}$$

The flow through the porous material is equal to the reduction in volume and is given by

$$\nabla \cdot v_d = -\bar{\alpha}\mathbf{m}^{\mathrm{T}} \frac{\partial \boldsymbol{\varepsilon}}{\partial t}. \tag{11}$$

The rate of change of grain volume due to pressure changes within the domain is given by

$$\left(\frac{\bar{\alpha} - n}{K_s} + \frac{n}{K_w}\right)\frac{\partial P_w}{\partial t}, \tag{12}$$

where K_w represents the bulk modulus of water, μ_w is the fluid viscosity and $\mathbf{K}_m$ is the material/matrix permeability. Equations (10)–(12) together define the continuity/mass balance equation that is given by

$$\left(\frac{\bar{\alpha} - n}{K_s} + \frac{n}{K_w}\right)\frac{\partial P_w}{\partial t} + \nabla \cdot \left(\frac{\mathbf{K}_m}{\mu_w}(-\nabla P_w + \rho \mathbf{g})\right) + \bar{\alpha}\mathbf{m}^{\mathrm{T}} \frac{\partial \boldsymbol{\varepsilon}}{\partial t} = 0. \tag{13}$$

3. INITIAL AND BOUNDARY CONDITIONS

Initial conditions that specify the displacements and water pressures at $t = 0$ are given by

$$\mathbf{u} = \mathbf{u}_0 \text{ in } \ \boldsymbol{\Omega} \cup \boldsymbol{\Gamma}, \tag{14}$$

$$P_w = P_w^0 \text{ in } \ \boldsymbol{\Omega} \cup \boldsymbol{\Gamma}, \tag{15}$$

where $\boldsymbol{\Omega}$ is the domain of interest and $\boldsymbol{\Gamma}$ its boundary. Boundary conditions can be imposed pressures on $\boldsymbol{\Gamma}_{field}$ (Dirichlet boundary conditions) or fluxes on $\boldsymbol{\Gamma}^q_{field}$ (Neumann boundary conditions), where the boundary $\boldsymbol{\Gamma} = \boldsymbol{\Gamma}_{field} \cup \boldsymbol{\Gamma}^q_{field}$. Dirichlet boundary conditions for displacements and pore water pressures are given by

$$\mathbf{u} = \hat{\mathbf{u}} \quad \text{on} \quad \boldsymbol{\Gamma}_u, \tag{16}$$

$$P_w = \hat{P}_w \ \text{ on } \ \boldsymbol{\Gamma}_w, \tag{17}$$

whereas Neumann boundary conditions for imposed stresses and flux conditions are as follows:

$$\overline{\mathbf{t}} = \mathbf{n} \cdot \boldsymbol{\sigma} \quad \text{on } \boldsymbol{\Gamma}^q_u, \tag{18}$$

$$q_w = \rho_w \frac{\mathbf{K}_m}{\mu_w}(-\nabla P_w + \rho_w \mathbf{g})^{\mathrm{T}} \cdot \mathbf{n} \quad \text{on } \ \boldsymbol{\Gamma}^q_w, \tag{19}$$

where $\mathbf{n}$ is the unit normal vector to the surface, $\overline{\mathbf{t}}$ is the prescribed external traction force and q_w is the applied mass flux normal to the boundary.

DOI: 10.1002/nag

Although it is appreciated that the simulation of large domains often involves unbounded continua and the use of Dirichlet/Neumann boundary conditions cannot realistically represent the far field deformation (mechanical) and fluid flow (hydraulic) interaction in an infinite domain [29–31], the use of these boundary conditions are considered adequate to demonstrate the validity of the proposed scheme.

4. FRACTURE MAPPING

This section presents the new FM approach that is used to capture flow interaction between the porous matrix and existing fractures [1]. In this approach, an element intersected by a fracture is treated as a superposition of two elements, a matrix and fracture element, which interact via a transfer function (see Figure 1). The transfer function provides a mathematical description of the fluid flow interaction between the matrix and the fracture. The function adopted in this study is based on the quasi steady-state function proposed by Barenblatt *et al.* [6], which assumes that the flow within an element is directly proportional to the difference between the matrix pore pressure and the fracture fluid pressure, that is,

$$T_r = \frac{\bar{\mathrm{s}}\mathbf{K}_f}{\mu_w}\left(P_{wm} - P_{wf}\right), \tag{20}$$

where $\mathbf{K}_f$ is the fracture permeability, μ_w is the fluid viscosity, P_{wm} is the matrix fluid pore pressure and P_{wf} is the fracture fluid pressure. The fracture permeability can be determined using the following relationship proposed by Witherspoon *et al.* [32]:

$$\mathbf{K}_f = \frac{b^2}{12}, \tag{21}$$

where b is the fracture width. In the original transfer function presented by Barenblatt *et al.* [6], $\bar{\mathrm{s}}$ represents a shape factor that is dependent on the width and geometry of existing fractures. Because the FM accounts for the width and geometry of a fracture within a fracture element, the shape factor is not required; however, it has been retained to ensure dimensional consistency when the transfer function is introduced into the coupled deformation and fluid flow formulation. The variable $\bar{\mathrm{s}}$ has dimension L^{-2}, where L represents length and has been assigned the value of 1.

The amount of the fluid transferred between the matrix and fracture elements is characterized by the fracture permeability $\mathbf{K}_f$. It should be noted that because fracture elements share mesh nodes with neighbouring fracture elements, the fluid pressure is continuous across these elements (see Figure 1).

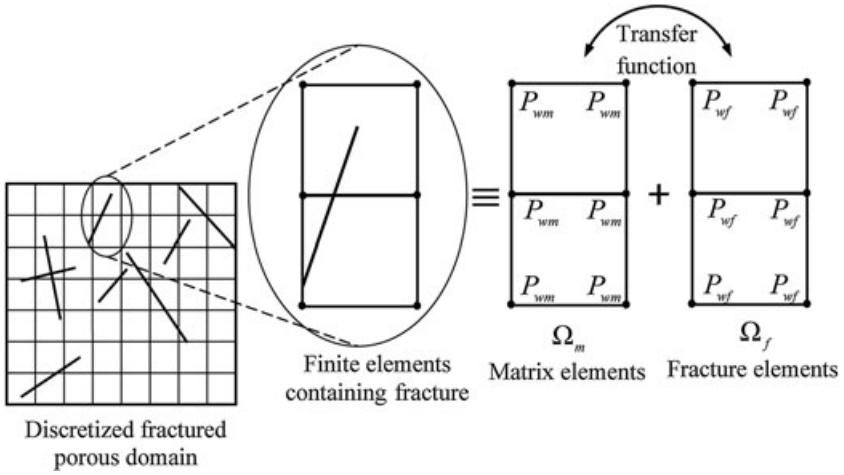

Figure 1. Schematic representation of the matrix and fracture elements/nodes extracted from discretized fractured domain.

DOI: 10.1002/nag

When fractures intersect within an element, the FM is accomplished by creating a fracture element for each fracture that exists within the element (see Figure 2).

The fracture permeability is represented within a fracture element through the following mapping:

$$\mathbf{K}_{fe} = \frac{A_f}{A_e}\mathbf{K}'_f, \tag{22}$$

where $\mathbf{K}_{fe}$ is the fracture element permeability, A_f is the area of the fracture within the element, A_e is the area of the element and $\mathbf{K}'_f$ is the fracture permeability tensor aligned to the global Cartesian axes (see Figure 3). This mapping equates the total flow through the fracture to the total flow through the fracture element and ensures an effective representation of the fracture flow within the fracture element.

5. FRACTURE REPRESENTATION

The LSM is commonly used in conjunction with XFEM to represent discontinuities instead of using an explicit representation [13, 23, 24, 28, 33–36]. In this work, it has been used to represent existing fractures. A fracture is represented as the zero level set of the signed distance function $\phi(\mathbf{x})$, that is, by

$$\phi(\mathbf{x}) = 0. \tag{23}$$

The signed distance function is defined by

$$\phi(\mathbf{x}) = \operatorname{sign}\left[\mathbf{n}\cdot\left(\mathbf{x}-\overline{\mathbf{x}}\right)\right] \min_{\overline{\mathbf{x}}\in\Gamma_{\mathrm{fr}}} \left\|\mathbf{x}-\overline{\mathbf{x}}\right\|, \tag{24}$$

where $\mathbf{x}$ is a finite element mesh node, $\overline{\mathbf{x}}$ is the normal projection of the point $\mathbf{x}$ onto the fracture defined by Γ_{fr} and $\mathbf{n}$ is the unit outward normal from the fracture at $\overline{\mathbf{x}}$ (see Figure 4). The fracture tips are defined by a tangential level set $\psi_i(\mathbf{x})$ given by

$$\psi_i(\mathbf{x}) = (\mathbf{x}-\mathbf{x}_i)\cdot\hat{\mathbf{t}}, \tag{25}$$

where $\hat{\mathbf{t}}$ is a unit vector tangent to the fracture at its tip and $\mathbf{x}_i$ is the location of the ith fracture tip. When more than one fracture tip exists in the domain, the tangential level set can be represented by a single function and given as

$$\psi(\mathbf{x}) = \max_i\ (\psi_i). \tag{26}$$

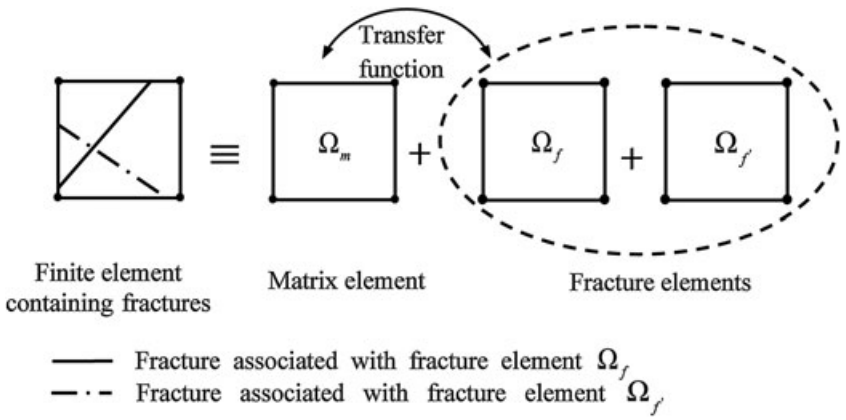

Figure 2. Schematic representation of fracture mapping for intersecting fractures.

DOI: 10.1002/nag

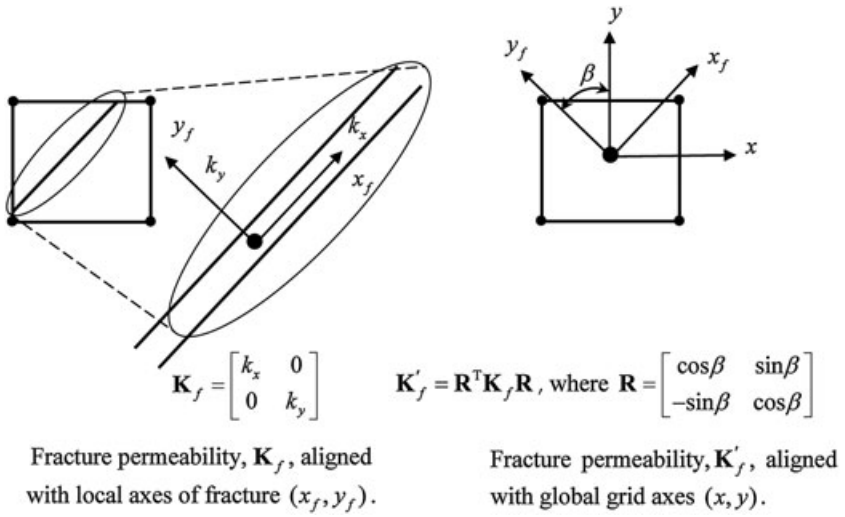

Figure 3. Fracture permeability is aligned with the Cartesian axes using the rotation tensor **R**.

By using the signed distance function and tangential level set, a fracture in 2D is defined by

$$\phi(\mathbf{x}) = 0 \text{ and } \psi(\mathbf{x}) \leq 0. \tag{27}$$

The level set functions $\phi(\mathbf{x})$ and $\psi_i(\mathbf{x})$ and the representation of the fracture are also illustrated in Figure 4.

6. ASSIGNMENT OF FRACTURED ELEMENTS

This section briefly illustrates how fractured elements are determined. For a given fracture, whose input geometry is defined by a single line segment or a series of line segments, the values of $\phi(\mathbf{x})$ and $\psi(\mathbf{x})$ are calculated for all the finite element nodes within close proximity to the fracture (see Figure 5). An element is defined as a fracture element if the values of $\phi(\mathbf{x})$ and $\psi(\mathbf{x})$ determined at its nodes satisfy the following conditions [24]:

$$\begin{cases} \phi_{\max}\phi_{\min} \leq 0, & \psi < 0, \text{ split element,} \\ \phi_{\max}\phi_{\min} \leq 0, & \psi_{\max}\psi_{\min} \leq 0, \text{ tip element.} \end{cases} \tag{28}$$

Split elements are defined as those elements that are completely cut by a fracture, and tip elements are those elements that contain a fracture tip. FM is applied to both split and tip elements.

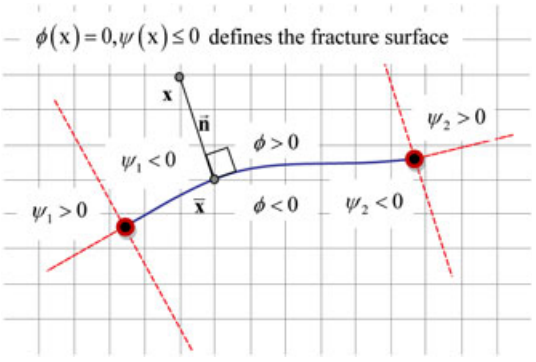

Figure 4. Level set fracture representation.

DOI: 10.1002/nag

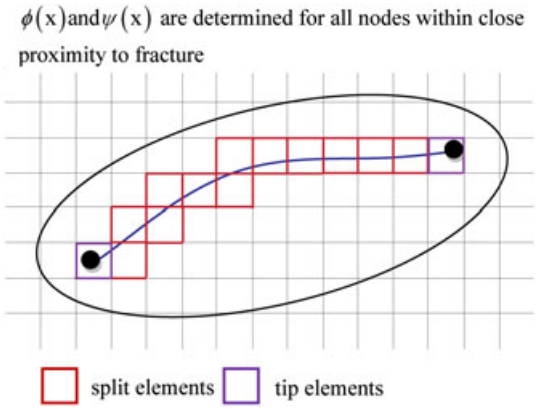

Figure 5. Assignment of fractured elements using level set values.

7. THE EXTENDED FINITE ELEMENT METHOD

The XFEM was introduced by Belytschko and Black [37] and exploits the partition of unity property of finite elements. Local enrichment functions are added to the finite element shape functions that allow the approximated field and its derivatives to be discontinuous within an element. Therefore, a domain can be modelled by finite elements without explicitly meshing discontinuities.

The enrichment terms consist of a modified Heaviside function and Branch functions that represent the Westergaard near tip asymptotic fields ([21, 38]). The Heaviside function is applied to elements entirely cut by a fracture and is given by

$$H(\mathbf{x}) = \begin{cases} +1 & \phi(\mathbf{x}) \geq 0, \\ -1 & \phi(\mathbf{x}) < 0, \end{cases} \tag{29}$$

where $\phi(\mathbf{x})$ is the signed distance function normal to the crack and Branch functions that represent the Westergaard near tip asymptotic fields [21, 38].

$$\left[\Phi_\gamma(\mathbf{x})\right]_{\gamma=1}^{4} = \left[\sqrt{r}\sin\frac{\theta}{2}, \sqrt{r}\cos\frac{\theta}{2}, \sqrt{r}\sin\theta\sin\frac{\theta}{2}, \sqrt{r}\sin\theta\cos\frac{\theta}{2}\right], \tag{30}$$

where r and θ are the polar coordinates of the point $\mathbf{x}$ (integration point or finite element node) in the coordinate system centred on the tip of the fracture with the x-axis aligned with the fracture direction (Figure 6).

The addition of these enrichment terms results in the following displacement field within a fractured domain:

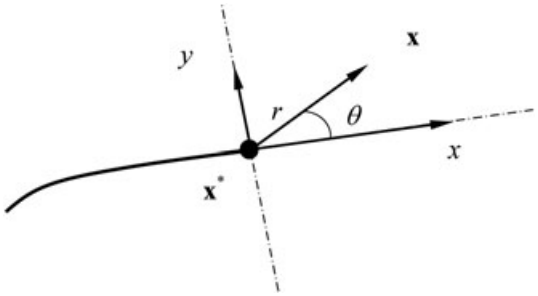

Figure 6. Coordinate configuration for fracture front enrichment functions in 2D. $\mathbf{x}^*$ represents the fracture tip, and $\mathbf{x}$ represents either an integration point or finite element node.

DOI: 10.1002/nag

$$\mathbf{u}(\mathbf{x}) = \underbrace{\sum_{I\in\mathcal{N}} N_u^I(\mathbf{x})\mathbf{u}_I}_{\text{Standard}} + \underbrace{\sum_{J\in\mathcal{N}_{\text{cr}}} \hat{N}_u^J(\mathbf{x})\,[H(\phi(\mathbf{x})) - H(\phi(\mathbf{x}_J))]\mathbf{a}_J}_{\text{Heaviside}} + \underbrace{\sum_{K\in\mathcal{N}_{\text{tip}}} \hat{N}_u^K(\mathbf{x}) \sum_{\gamma=1}^{4} (\mathbf{x}) \left[\Phi_\gamma(\mathbf{x}) - \Phi_\gamma(\mathbf{x}_K)\right]\mathbf{b}_{\gamma K}}_{\text{Branch}}, \tag{31}$$

where $\mathbf{u}_I$ is the nodal displacement vector associated with the continuous part of the finite element solution (standard approximation), N_u^I, $\hat{N}_u^J$ and $\hat{N}_u^K$ are finite element shape functions, $\mathcal{N}$ is the set of all nodes in the mesh, $\mathcal{N}_{\text{cr}}$ is the set of nodes whose support element is cut by the fracture and $\mathcal{N}_{\text{tip}}$ is the set of nodes whose support element contains a fracture tip. $\mathbf{a}_J$ is the nodal enriched degrees of freedom vector associated with the modified Heaviside function, and $\mathbf{b}_{\gamma K}$ is the nodal enriched degree of freedom vector associated with the elastic asymptotic fracture tip functions. Both $\mathbf{a}_J$ and $\mathbf{b}_{\gamma K}$ represent additional degrees of freedom associated with enriched nodes.

The determination of both Heaviside and tip enriched nodes is illustrated in Figure 7. Tip enriched nodes can be determined via topological or geometrical/fixed area enrichment. Only the nodes of elements containing the fracture tips are enriched if topological enrichment is implemented. If geometrical enrichment is used, nodes within a fixed area centred on the fracture tip become tip enriched nodes (see Figure 7). Although topological enrichment is usually adequate, geometrical enrichment improves the method's rate of convergence [39–41]. Geometrical enrichment was used for the numerical example presented in this paper with a fixed area of radius (**R**) 1/20 of the domain width.

8. NUMERICAL INTEGRATION

Standard Gaussian integration causes numerical inaccuracies and creates ill-conditioned system matrices when performed on elements enriched by the discontinuous Heaviside function (29) and Branch functions (30) [40, 42, 43]. To remedy the numerical issues associated with the integration of these discontinuous enrichment functions, elements intersected by a fracture are decomposed into sub-elements. The edges of these sub-elements are aligned along the discontinuity surface, and a higher order of Gaussian quadrature is used in these elements to improve the accuracy of the numerical integration.

Element decomposition is carried out only for the purpose of numerical integration and does not introduce any additional degrees of freedom (nodes) to the discretized domain. Decomposition of finite elements that are intersected by a fracture is a straightforward procedure that is carried out using computational geometry because no restrictions are placed on the shape of the generated sub-elements. Figure 8 illustrates element decomposition for quadrilateral and triangular elements.

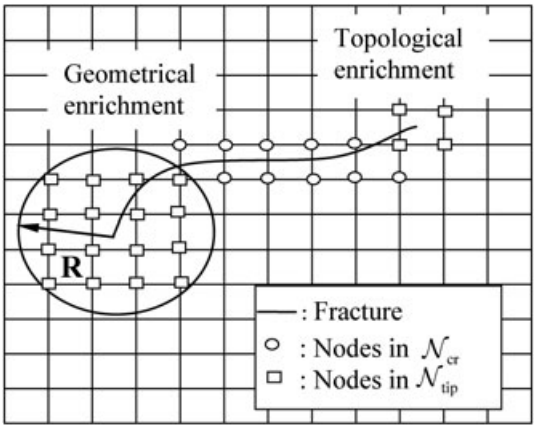

Figure 7. Assignment of enriched nodes. ○, Heaviside enriched; □, tip enriched.

DOI: 10.1002/nag

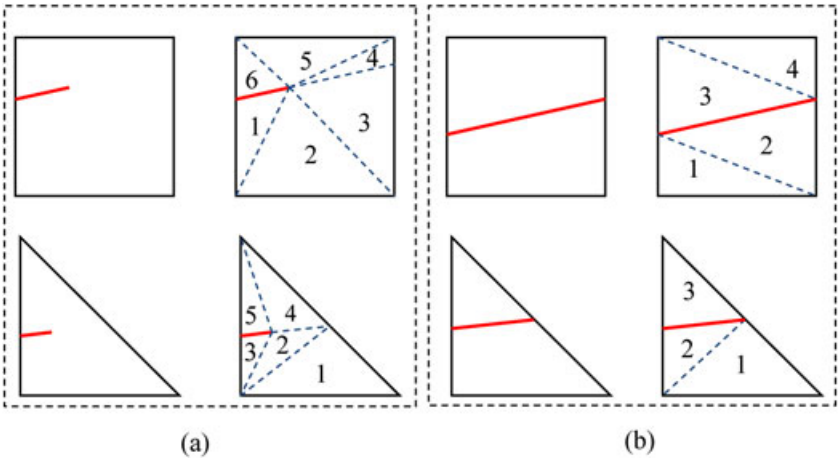

Figure 8. Element decomposition into sub-elements: (a) elements containing fracture tip and (b) elements completely cut by fracture.

9. SPATIAL DISCRETIZATION

The discrete equations are obtained by applying the Galerkin-based finite element approach to the governing and continuity equations. To simplify the discretized system equations, the effect of gravity is neglected, and the material grains are assumed incompressible, that is, Biot's compressibility coefficient, $\bar{\alpha}$, is equal to 1. Before discretization, the transfer function term that accounts for the fluid flow interaction between the matrix and fracture, and a source/sink term are introduced to the continuity equation, which then takes the form

$$\nabla\cdot\left(-\frac{\mathbf{K}_m}{\mu_w}\nabla P_w\right)+\frac{\bar{s}\mathbf{K}_f}{\mu_w}\left(P_{wm}-P_{wf}\right)+Q_w+\frac{n}{K_w}\frac{\partial P_w}{\partial t}+\mathbf{m}^{\mathrm{T}}\frac{\partial\boldsymbol{\varepsilon}}{\partial t}=0. \tag{32}$$

After Ghafouri and Lewis ([14]), the continuity equations can be written for both the porous matrix and the fractures as

$$\nabla\cdot\left(-\frac{\mathbf{K}_m}{\mu_w}\nabla P_{wm}\right)+\frac{\bar{s}\mathbf{K}_f}{\mu_w}\left(P_{wm}-P_{wf}\right)+Q_w+\frac{n_m}{K_w}\frac{\partial P_{wm}}{\partial t}+\mathbf{m}^{\mathrm{T}}\frac{\partial\boldsymbol{\varepsilon}}{\partial t}=0 \tag{33}$$

for the porous matrix and

$$\nabla\cdot\left(-\frac{\mathbf{K}_f}{\mu_w}\nabla P_{wf}\right)-\frac{\bar{s}\mathbf{K}_f}{\mu_w}\left(P_{wm}-P_{wf}\right)+\frac{n_f}{K_w}\frac{\partial P_{wf}}{\partial t}=0 \tag{34}$$

for the fractured zone. When solving Equations (33) and (34), boundary conditions are only applied to the matrix domain. These boundary conditions can be either Dirichlet or Neumann boundary conditions. Enforcing Dirichlet boundary conditions involves specifying displacements and/or pressures at the matrix domain boundaries. Neumann boundary conditions require the specification of stresses and/or flow rates at the domain boundaries.

The dependent pressure variables are approximated by

$$\begin{aligned}P_{wm}&=\mathbf{N}_p\bar{\mathbf{P}}_{wm},\\ P_{wf}&=\mathbf{N}_p\bar{\mathbf{P}}_{wf},\end{aligned} \tag{35}$$

where $\bar{\mathbf{P}}_{wm}$ and $\bar{\mathbf{P}}_{wf}$ are the vectors of nodal unknowns of matrix and fracture excess pressures, respectively, and $\mathbf{N}_p$ is the approximating shape function. A second-order polynomial is used as the displacement shape function, $\mathbf{N}_u$, whereas a first-order polynomial is used for the pressure, $\mathbf{N}_p$. This element pair satisfies the Babuška–Brezzi convergence condition, particularly when approaching the

DOI: 10.1002/nag

undrained limit state [29, 44–46]. A combination of eight-noded quadratic and bi-linear elements is used for the numerical tests carried out in this paper (Figure 9). Displacements are calculated at the element vertices, and mid-side nodes of the quadratic elements and pressures are calculated at the vertices of the linear elements.

It is important to note that a first-order polynomial is also used for the shape function of the discontinuous part of (31), $\hat{\mathbf{N}}_u$ (see Figure 9(a)). Stazi *et al*. [34] demonstrated that this combination of a higher-order shape function for the continuous portion of the enriched approximation performs well within the XFEM framework.

The resulting spatial discretization takes the form

$$\mathbf{A}\mathbf{X} + \mathbf{B}\frac{\mathbf{dX}}{\mathbf{dt}} = \mathbf{C}, \tag{36}$$

where

$$\mathbf{A} = \begin{bmatrix} 0 & 0 & 0 & 0 & 0 \\ 0 & 0 & 0 & 0 & 0 \\ 0 & 0 & 0 & \mathbf{H}_m + \mathbf{H}_{Tr} & -\mathbf{H}_{Tr} \\ 0 & 0 & 0 & -\mathbf{H}_{Tr} & \mathbf{H}_f + \mathbf{H}_{Tr} \end{bmatrix}, \tag{37}$$

$$\mathbf{B} = \begin{bmatrix} \mathbf{Ke}_{uu} & \mathbf{Ke}_{ua} & \mathbf{Ke}_{ub} & -\mathbf{L} & 0 \\ \mathbf{Ke}_{au} & \mathbf{Ke}_{aa} & \mathbf{Ke}_{ab} & -\mathbf{L}_a & 0 \\ \mathbf{Ke}_{bu} & \mathbf{Ke}_{ba} & \mathbf{Ke}_{bb} & -\mathbf{L}_b & 0 \\ \mathbf{L}^{\mathrm{T}} & \mathbf{L}_a^{\mathrm{T}} & \mathbf{L}_b^{\mathrm{T}} & \mathbf{S}_m & 0 \\ 0 & 0 & 0 & 0 & \mathbf{S}_f \end{bmatrix}, \tag{38}$$

$$\mathbf{X} = \begin{bmatrix} \mathbf{u} \\ \mathbf{a} \\ \mathbf{b} \\ \overline{\mathbf{P}}_{wm} \\ \overline{\mathbf{P}}_{wf} \end{bmatrix}, \tag{39}$$

$$\mathbf{C} = \begin{bmatrix} \mathrm{d}\mathbf{F} \\ \mathrm{d}\mathbf{F}_a \\ \mathrm{d}\mathbf{F}_b \\ \overline{\mathbf{f}} \\ 0 \end{bmatrix}. \tag{40}$$

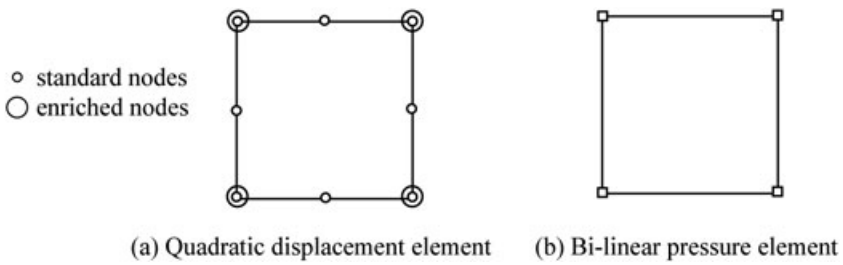

Figure 9. Element combination used for interpolation of the coupled solid–fluid interaction. (a) Quadratic elements are used for displacement with enriched vertices, and (b) bi-linear elements are used for pressure. The pressure field is treated as continuous in each domain; therefore, no enrichment is required.

DOI: 10.1002/nag

Elements of the aforementioned listed matrices are given in Appendix A.

10. TEMPORAL DISCRETIZATION

Using an implicit time discretization scheme with the following approximations:

$$\left(\frac{d\mathbf{X}}{dt}\right)_{n+\theta} = \frac{\mathbf{X}_{n+1} - \mathbf{X}_n}{\Delta t}, \tag{41}$$

$$\mathbf{X}_{n+\theta} = (1-\theta)\mathbf{X}_n + \theta\mathbf{X}_{n+1}. \tag{42}$$

Then, substituting (41) and (42) into (36) produces

$$(\mathbf{B} + \mathbf{A}\Delta t\theta)\mathbf{X}_{n+1} = (\mathbf{B} - \mathbf{A}\Delta t(1-\theta))\mathbf{X}_n + \mathbf{C}\Delta t. \tag{43}$$

The final discrete equations can be written as

$$\begin{bmatrix} \mathbf{Ke}_{uu} & \mathbf{Ke}_{ua} & \mathbf{Ke}_{ub} & -\mathbf{L} & 0 \\ \mathbf{Ke}_{au} & \mathbf{Ke}_{aa} & \mathbf{Ke}_{ab} & -\mathbf{L}_a & 0 \\ \mathbf{Ke}_{bu} & \mathbf{Ke}_{ba} & \mathbf{Ke}_{bb} & -\mathbf{L}_b & 0 \\ \mathbf{L}^{\mathrm{T}} & \mathbf{L}_a^{\mathrm{T}} & \mathbf{L}_b^{\mathrm{T}} & \Delta t\theta(\mathbf{H}_m + \mathbf{H}_{Tr}) + \mathbf{S}_m & -\mathbf{H}_{Tr}\Delta t\theta \\ 0 & 0 & 0 & -\mathbf{H}_{Tr}\Delta t\theta & \left(\mathbf{H}_f + \mathbf{H}_{Tr}\right)\Delta t\theta + \mathbf{S}_f \end{bmatrix} \begin{bmatrix} \mathbf{u} \\ \mathbf{a} \\ \mathbf{b} \\ \mathbf{P}_{wm} \\ \mathbf{P}_{wf} \end{bmatrix}_{n+1}$$

$$= \begin{bmatrix} \mathbf{Ke}_{uu} & \mathbf{Ke}_{ua} & \mathbf{Ke}_{ub} & -\mathbf{L} & 0 \\ \mathbf{Ke}_{au} & \mathbf{Ke}_{aa} & \mathbf{Ke}_{ab} & -\mathbf{L}_a & 0 \\ \mathbf{Ke}_{bu} & \mathbf{Ke}_{ba} & \mathbf{Ke}_{bb} & -\mathbf{L}_b & 0 \\ \mathbf{L}^{\mathrm{T}} & \mathbf{L}_a^{\mathrm{T}} & \mathbf{L}_b^{\mathrm{T}} & \mathbf{S}_m - \Delta t(1-\theta)(\mathbf{H}_m + \mathbf{H}_{Tr}) & \mathbf{H}_{Tr}\Delta t(1-\theta) \\ 0 & 0 & 0 & \mathbf{H}_{Tr}\Delta t(1-\theta) & \mathbf{S}_f - \left(\mathbf{H}_f + \mathbf{H}_{Tr}\right)\Delta t(1-\theta) \end{bmatrix} + \begin{bmatrix} d\mathbf{F} \\ d\mathbf{F}_a \\ d\mathbf{F}_b \\ \mathbf{f} \\ 0 \end{bmatrix} \Delta t. \tag{44}$$

The value of θ determines the accuracy and stability of the time integration scheme. When $\theta = 1$, the scheme is fully implicit (backward Euler) and imposes no requirements on the time step size (Δt) chosen for both stability and the elimination oscillatory effects in the solution. The fully implicit scheme has been implemented in the numerical tests conducted in this paper.

11. FM-XFEM IMPLEMENTATION

This section summarizes the implementation procedure for the FM/XFEM method. The method implementation has the following steps:

1. Generate mesh: the domain is divided into a series of finite elements.
2. Calculate the level sets of nodes in the vicinity of the line segments that describe the fracture geometry. Nodal enrichment is also assigned at this step.
3. Determine fracture elements using the equality conditions discussed in Section 6.
4. Loop over all elements (matrix assembly):
   a. Determine element contributions to discrete system equation (44): if an element is a fracture element, calculate element permeability using the procedure. Element contributions are also made to the fracture permeability and transfer matrix ($\mathbf{H}_f$ and $\mathbf{H}_{Tr}$) for fracture elements.
   b. Add element contributions to the global system matrix.
5. Apply boundary conditions.
6. Solve the system equations given by (44) to obtain field variables, nodal displacements and pressures, at each time step.

This implementation procedure assumes that the fracture geometry remains constant over the simulation period. Both the matrix and fracture permeabilities are also assumed constant.

DOI: 10.1002/nag

12. NUMERICAL EXAMPLE

The validity of the FM-XFEM model is demonstrated on a 2D plane strain problem shown in Figure 10. The domain is fully saturated and allowed to freely drain at the top, that is, excess pore water pressure is equal to zero. The domain is assumed to be sealed on the right, left and basal boundaries. A static load of 10 kN/m^2 is applied at the top of the block at time $t=0$ and maintained throughout the duration of the simulation. The block is homogenous and assumed to behave in a linearly elastic manner with the material properties shown in Table I. The fracture is 8 m long, is inclined at a 45° angle and is centred in the middle of the block. The fracture is assumed traction free, that is, contact forces are neglected.

The current model is compared with a standard finite element model (SFEM) in which the fracture is modelled as an elliptical soft inclusion with its interior meshed along with the domain using Taylor–Hood elements (triangular six/three node element pair-T6/T3). The inclusion has an aspect ratio of ~1:40 with a Young's modulus three orders of magnitude lower than the surrounding matrix material and a Poisson's ratio of $\nu=0$. Because the fracture geometry remains constant throughout the simulation for the FM-XFEM model, that is, the fracture does not close or open during the simulation, the nodes of the elements used to model the soft inclusion are assigned a cross-displacement of zero to ensure consistency between the SFEM and FM-XFEM models.

The computational meshes used for the both the SFEM and FM-XFEM are shown in Figure 11 along with the level of refinement used around the tip of the fracture in the SFEM mesh. A uniform mesh was used for the FM-XFEM to demonstrate the method's ability to produce fairly accurate results in the vicinity of the discontinuity without the need for mesh refinement.

The resulting displacement fields after 100 days are shown in Figure 12, and they are qualitatively identical. The vertical displacement at A (point located at the surface shown in Figure 10) during 100 days is given in Figure 13. The plot also illustrates the displacement variation for the SFEM

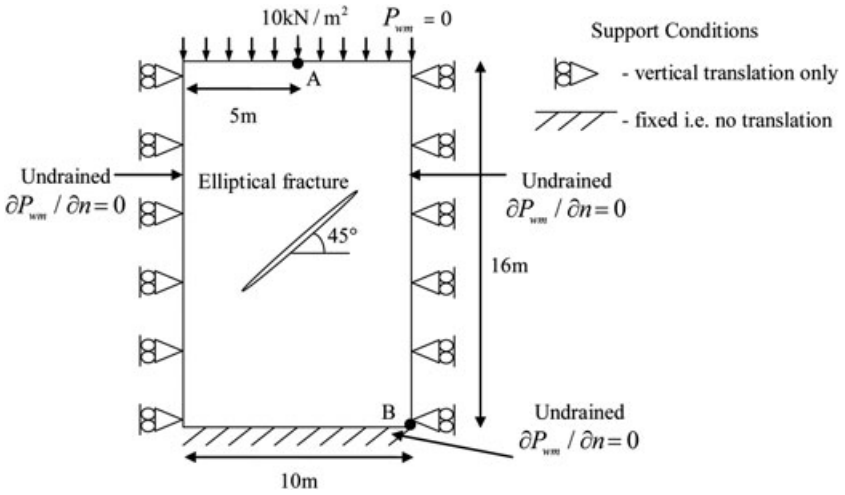

Figure 10. Two-dimensional fractured domain with assigned boundary conditions.

Table I. Material properties.

Parameter	Definition	Magnitude	Units
E	Modulus of elasticity	40	MPa
ν	Poisson's ratio	0.3	—
n_m	Matrix porosity	0.1	—
n_f	Fracture porosity	0.05	—
$\mathbf{K}_m/\mu$	Matrix mobility	1×10^{-6}	m^4/(MNs)
$\mathbf{K}_f/\mu$	Fracture mobility	1×10^{-1}	m^4/(MNs)

DOI: 10.1002/nag

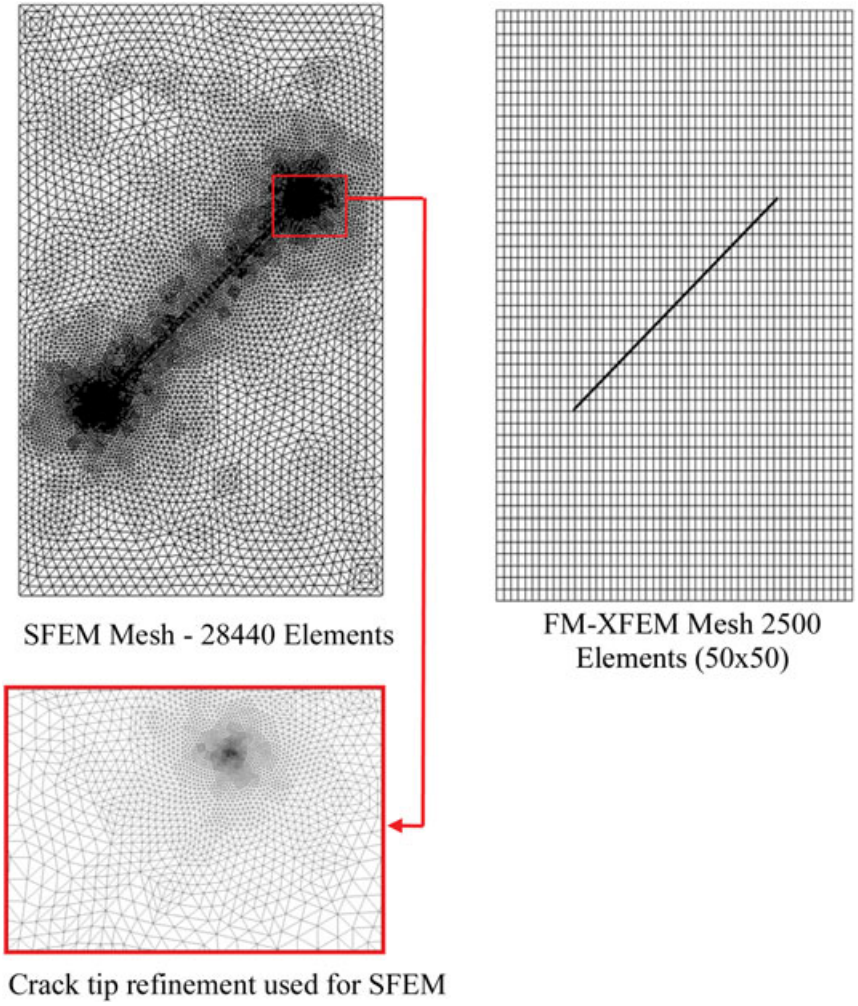

Figure 11. Computational meshes used to conduct method comparison.

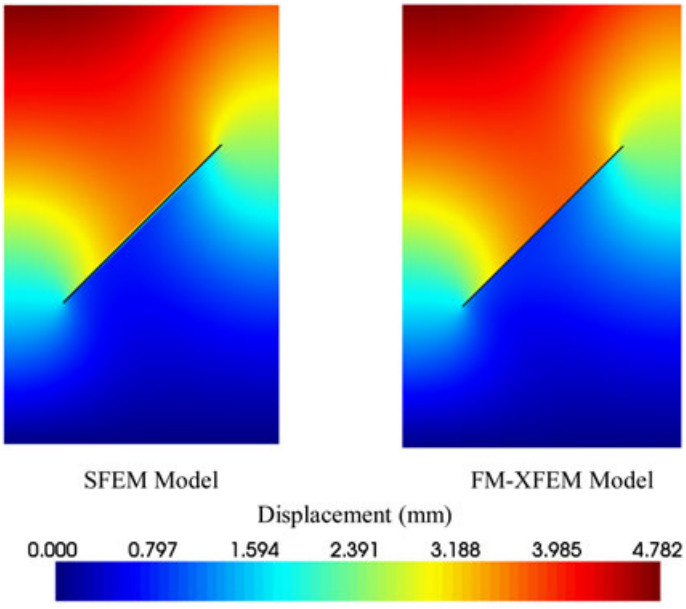

Figure 12. Displacement field after 100 days for SFEM and FM-XFEM.

DOI: 10.1002/nag

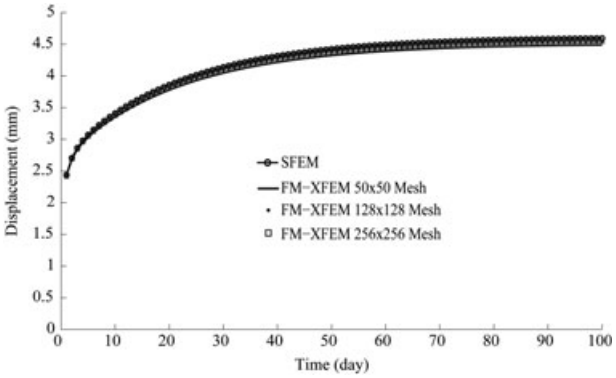

Figure 13. Surface displacement at point A obtained for SFEM and FM-XFEM.

model and the current method at varying mesh resolutions. The FM-XFEM results adequately match the results of the SFEM model and show very little change in the resulting displacement at higher mesh resolutions.

The excess pore pressure fields are given in Figure 14, and they are also qualitatively identical. The variation in the excess pore pressure within the domain at point B (point located at basal boundary shown in Figure 10) has been plotted in Figure 15. The plot shows the variation in pressure for the SFEM and the current model at varying mesh resolutions. The pressure variation is essentially identical for all mesh resolutions used for the FM-XFEM and the SFEM results.

A point of interest observed on the pore pressure plot of both models is the increase in the initial pressure before it starts to dissipate. The increase in excess pore pressure from the initial pressure and then the decrease are described as the Mandel–Cryer effect [47, 48]. The initial contraction of the domain that occurs as the fluid rapidly escapes the top of the domain causes an increase in the excess pore pressure above the initial value. The results obtained illustrate that on a coarse mesh, FM-XFEM, is able to provide a physical description of the pressure dissipation comparable with that of the SFEM.

The rate of convergence of the FM-XFEM has also been determined using this 2D plane strain example. In the absence of an exact solution for this particular problem, a reference solution obtained on a 512×512 mesh was used to represent the exact solution, and mesh resolutions used to determine the rate of convergence were 32×32, 64×64, 128×128 and 256×256. The error

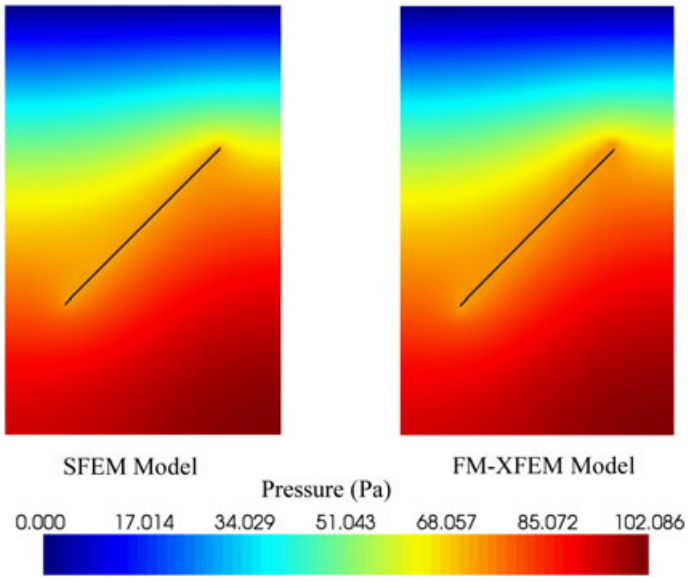

Figure 14. Excess pore pressure field after 100 days for SFEM and FM-XFEM.

DOI: 10.1002/nag

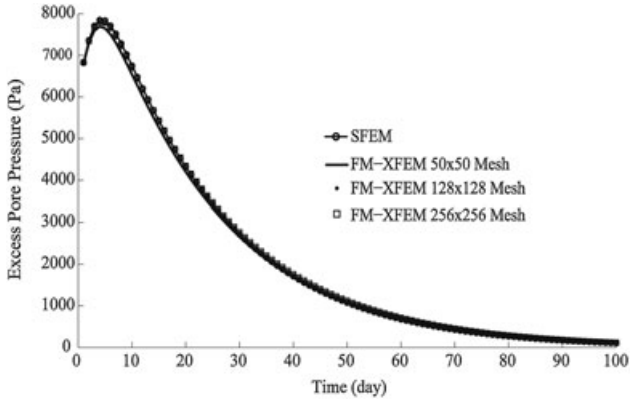

Figure 15. Excess pore pressure at point B obtained for SFEM and FM-XFEM.

measure of the coupled formulation was calculated as the sum of the L_2-norm of the displacement gradients and the L_2-norm of the pressure given by [49]

$$\|\mathbf{u}_{ex} - \mathbf{u}_{num}\|_1 + \|\mathbf{p}_{ex} - \mathbf{p}_{num}\|_0 = O\left(h^{\min(k,l+1)}\right), \tag{45}$$

where $\mathbf{u}_{ex}$ and $\mathbf{p}_{ex}$ are the exact values of the displacement and pressure, respectively, $\mathbf{u}_{num}$ and $\mathbf{p}_{num}$ are the numerically determined displacement and pressure values, respectively, k and l are the orders of the displacement and pressure interpolations and have the values of 2 and 1, respectively.

The norms in (45) are given by

$$\|\mathbf{u}_{ex} - \mathbf{u}_{num}\|_1 = \left(\int_\Omega (\mathbf{u}_{ex} - \mathbf{u}_{num})^2 + (\nabla \mathbf{u}_{ex} - \nabla \mathbf{u}_{num})^2 \mathrm{d}\Omega \right)^{1/2}, \tag{46}$$

$$\|\mathbf{p}_{ex} - \mathbf{p}_{num}\|_0 = \left(\int_\Omega (\mathbf{p}_{ex} - \mathbf{p}_{num})^2 d\Omega \right)^{1/2}. \tag{47}$$

These norms are normalized by the norm of the exact solution before determining the rate of convergence and are given by [50]

$$\frac{\|\mathbf{u}_{ex} - \mathbf{u}_{num}\|_1}{\|\mathbf{u}_{ex}\|_1} = \frac{\left(\int_\Omega (\mathbf{u}_{ex} - \mathbf{u}_{num})^2 + (\nabla \mathbf{u}_{ex} - \nabla \mathbf{u}_{num})^2 d\Omega \right)^{1/2}}{\left(\int_\Omega (\mathbf{u}_{ex})^2 + (\nabla \mathbf{u}_{ex})^2 d\Omega \right)^{1/2}}, \tag{48}$$

$$\frac{\|\mathbf{p}_{ex} - \mathbf{p}_{num}\|_0}{\|\mathbf{p}_{ex}\|_0} = \frac{\left(\int_\Omega (\mathbf{p}_{ex} - \mathbf{p}_{num})^2 d\Omega \right)^{1/2}}{\left(\int_\Omega (\mathbf{p}_{ex})^2 d\Omega \right)^{1/2}}. \tag{49}$$

The rate of convergence is given by the gradient of the log–log plot of the L_2 error norm versus the nodal spacing h. The rate of convergence obtained for the FM-XFEM scheme is 1.05. A log–log plot of the L_2 error norm versus the maximum nodal spacing h is shown in Figure 16.

DOI: 10.1002/nag

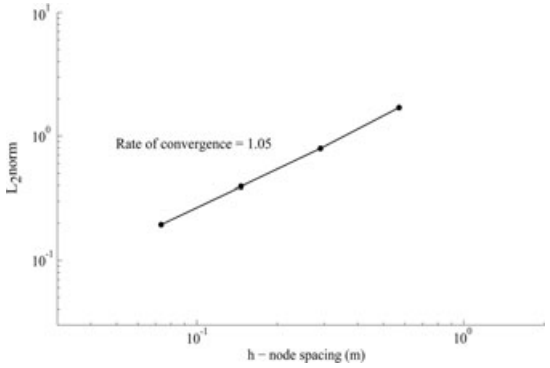

Figure 16. Convergence rate of FM-XFEM.

13. CONCLUSION

A new scheme for coupled deformation and fluid flow that combines a new FM approach and the XFEM has been presented. FM is used to account for the fluid flow interaction between the porous matrix and existing fractures, whereas the XFEM handles the discontinuous displacement field that exists across fractures. FM-XFEM is able to adequately determine the fluid flow and deformation in porous media without the need to explicitly mesh fractures within the computational domain. Although the method has been developed within a dual continuum framework, the flow through individual fractures is captured through permeability mapping. The validation exercise performed illustrates the method's potential as a viable continuum approach for simulating coupled fluid flow and deformation in fractured porous media including the propagation of individual fractures. The method also performs very well on coarse meshes.

APPENDIX A

$$\mathbf{Ke}_{uu} = -\int_{\Omega} \mathbf{B}^{\mathrm{T}}\mathbf{D}\mathbf{B}d\mathbf{\Omega}_m, \tag{50}$$

$$\mathbf{Ke}_{ua} = -\int_{\Omega} \mathbf{B}^{\mathrm{T}}\mathbf{D}\mathbf{B}^{a}d\mathbf{\Omega}_m, \tag{51}$$

$$\mathbf{Ke}_{ub} = -\int_{\Omega} \mathbf{B}^{\mathrm{T}}\mathbf{D}\mathbf{B}^{b}d\mathbf{\Omega}_m, \tag{52}$$

$$\mathbf{Ke}_{au} = -\int_{\Omega} \mathbf{B}^{a^{\mathrm{T}}}\mathbf{D}\mathbf{B}d\mathbf{\Omega}_m, \tag{53}$$

$$\mathbf{Ke}_{aa} = -\int_{\Omega} \mathbf{B}^{a^{\mathrm{T}}}\mathbf{D}\mathbf{B}^{a}d\mathbf{\Omega}_m, \tag{54}$$

$$\mathbf{Ke}_{ab} = -\int_{\Omega} \mathbf{B}^{a^{\mathrm{T}}}\mathbf{D}\mathbf{B}^{b}d\mathbf{\Omega}_{\mathrm{m}}, \tag{55}$$

$$\mathbf{Ke}_{bu} = -\int_{\Omega} \mathbf{B}^{b^{\mathrm{T}}}\mathbf{D}\mathbf{B}d\mathbf{\Omega}_m, \tag{56}$$

DOI: 10.1002/nag

$$\mathbf{Ke}_{ba} = -\int_{\Omega} \mathbf{B}^{b\mathrm{T}}\mathbf{D}\mathbf{B}^{a} d\mathbf{\Omega}_m, \tag{57}$$

$$\mathbf{Ke}_{bb} = -\int_{\Omega} \mathbf{B}^{b\mathrm{T}}\mathbf{D}\mathbf{B}^{b} d\mathbf{\Omega}_m, \tag{58}$$

$$\mathbf{L} = \int_{\Omega} \mathbf{B}^{\mathrm{T}}\mathbf{m}\mathbf{N}_p d\mathbf{\Omega}_{\mathrm{m}}, \tag{59}$$

$$\mathbf{L}_a = \int_{\Omega} \mathbf{B}^{a^{\mathrm{T}}}\mathbf{m}\mathbf{N}_p d\mathbf{\Omega}_m, \tag{60}$$

$$\mathbf{L}_b = \int_{\Omega} \mathbf{B}^{b\mathrm{T}}\mathbf{m}\mathbf{N}_p d\mathbf{\Omega}_m, \tag{61}$$

$$\mathbf{F} = -\int_{\Omega} \mathbf{N}_u^{\mathrm{T}} \rho \mathbf{g}\, d\mathbf{\Omega}_m - \int_{\Gamma} \mathbf{N}_u^{T}\, \overline{\mathbf{t}}\, d\mathbf{\Gamma}_m, \tag{62}$$

$$\mathbf{F}_a = -\int_{\Omega} H\mathbf{N}_u^{\mathrm{T}} \rho \mathbf{g} d\mathbf{\Omega}_m - \int_{\Gamma} H\mathbf{N}_u^{\mathrm{T}}\, \overline{\mathbf{t}}\, d\mathbf{\Gamma}_m, \tag{63}$$

$$\mathbf{F}_b = -\int_{\Omega} \Phi_\gamma \mathbf{N}_u^{\mathrm{T}} \rho \mathbf{g}\, d\mathbf{\Omega}_m - \int_{\Gamma} \Phi_\gamma \mathbf{N}_u^{\mathrm{T}} \overline{\mathbf{t}}\, d\mathbf{\Gamma}_m, \tag{64}$$

$$\mathbf{H}_m = \int_{\Omega} \left(\nabla \mathbf{N}_p\right)^{\mathrm{T}} \frac{\mathbf{K}_m}{\mu_w} \nabla \mathbf{N}_p d\mathbf{\Omega}_m, \tag{65}$$

$$\mathbf{H}_f = \int_{\Omega} \left(\nabla \mathbf{N}_p\right)^{\mathrm{T}} \frac{\mathbf{K}_f}{\mu_w} \nabla \mathbf{N}_p d\mathbf{\Omega}_m, \tag{66}$$

$$\mathbf{H}_{Tr} = \int_{\Omega} \mathbf{N}_p^{\mathrm{T}} \frac{\overline{\mathrm{s}}\mathbf{K}_f}{\mu_w} \mathbf{N}_p d\mathbf{\Omega}_{m\&f}, \tag{67}$$

$$\mathbf{S}_m = \int_{\Omega} \mathbf{N}_p^{\mathrm{T}} \frac{n_m}{K_w} \mathbf{N}_p d\mathbf{\Omega}_m, \tag{68}$$

$$\mathbf{S}_f = \int_{\Omega} \mathbf{N}_p^{\mathrm{T}} \frac{n_f}{K_w} \mathbf{N}_p d\mathbf{\Omega}_f, \tag{69}$$

$$\overline{\mathbf{f}} = \int_{\Gamma_w^q} \mathbf{N}_p^{\mathrm{T}} \frac{\mathbf{K}_m}{\mu_w} \rho_w \mathbf{g}\cdot\mathbf{n}\, d\mathbf{\Gamma}_m - \int_{\Gamma_w^q} \mathbf{N}_p^{\mathrm{T}} \frac{q_w}{\rho_w}\, d\mathbf{\Gamma}_m, \tag{70}$$

DOI: 10.1002/nag

$$\mathbf{B} = \nabla_s \mathbf{N}_u = \begin{bmatrix} \frac{\partial}{\partial x} & 0 \\ 0 & \frac{\partial}{\partial x} \\ \frac{\partial}{\partial y} & \frac{\partial}{\partial x} \end{bmatrix} \mathbf{N}_u, \tag{71}$$

$$\mathbf{B}^a = \nabla_s \hat{\mathbf{N}}_u (H(\phi(\mathbf{x})) - H(\phi(\mathbf{x}))) = \begin{bmatrix} \frac{\partial}{\partial x} & 0 \\ 0 & \frac{\partial}{\partial x} \\ \frac{\partial}{\partial y} & \frac{\partial}{\partial x} \end{bmatrix} \hat{\mathbf{N}}_u (H(\phi(\mathbf{x})) - H(\phi(\mathbf{x}))), \tag{72}$$

$$\mathbf{B}^b = \nabla_s \hat{\mathbf{N}}_u \big(\Phi_\gamma(\mathbf{x}) - \Phi_\gamma(\mathbf{x}_K)\big) = \begin{bmatrix} \frac{\partial}{\partial x} & 0 \\ 0 & \frac{\partial}{\partial x} \\ \frac{\partial}{\partial y} & \frac{\partial}{\partial x} \end{bmatrix} \hat{\mathbf{N}}_u \big(\Phi_\gamma(\mathbf{x}) - \Phi_\gamma(\mathbf{x}_K)\big), \tag{73}$$

$$\nabla \mathbf{N}_p = \begin{bmatrix} \frac{\partial}{\partial x} \mathbf{N}_p \\ \frac{\partial}{\partial y} \mathbf{N}_p \end{bmatrix}. \tag{74}$$

ACKNOWLEDGEMENTS

The first author would like to thank Total E&P UK Limited for sponsoring this work via a studentship grant. Gerard Gorman gratefully acknowledges support from the Leverhulme Trust. This work has also benefited from insightful discussions held with Dr. Rafid Al-Khoury and Prof. Martin Blunt during its initial stages and the wealth of experience in XFEM shared by Prof. Stéphane Bordas.

REFERENCES

1. Lamb AR, Gorman G, Gosselin OR, Onaisi A, Coupled deformation and fluid flow in fractured porous media using dual permeability and explicitly defined fracture geometry, in SPE EUROPEC/EAGE Annual Conference and Exhibition. 2010, Society of Petroleum Engineers: Barcelona, Spain.
2. Minkoff SE, Stone CM, Bryant S, Peszynska M, Wheeler MF. Coupled fluid flow and geomechanical deformation modeling. *Journal of Petroleum Science and Engineering* 2003; **38**(1-2):37–56.
3. Biot MA. General theory of three-dimensional consolidation. *Journal of Applied Physics* 1941; **12**(2):155–164.
4. Bai M, Elsworth D. *Coupled processes in subsurface deformation, flow, and transport*. American Society of Civil Engineers: Reston, VA, 2000 **xx**; 334.
5. Elsworth D, Bai M. Flow-deformation response of dual-porosity media. *Journal of Geotechnical Engineering-Asce* 1992; **118**(1):107–124.
6. Barenblatt GI, Zheltov IP, Kochina IN. Basic concepts in the theory of seepage of homogeneous liquids in fissured rocks [strata]. *Journal of Applied Mathematics and Mechanics* 1960; **24**(5):1286–1303.
7. Warren JE, Root PJ. The behavior of naturally fractured reservoirs. *SPE Journal* 1963; **3**(3):245–255. SPE 426-PA.
8. Karimi-Fard M, Durlofsky LJ, Aziz K. An efficient discrete-fracture model applicable for general-purpose reservoir simulators. *SPE Journal* 2004; **9**(2):227–236. SPE 88812-PA.
9. Kim JG, Deo D. Finite element, discrete-fracture model for multiphase flow in porous media. *AICHE Journal* 2000; **46**(6):1120–1130.
10. Tran NH, Ravoof A. Coupled fluid flow through discrete fracture network: a novel approach. *International Journal of Mathematics and Computers in Simulation* 2007; **1**(3):295–299.
11. Lee J, Choi S-U, Cho W. A comparative study of dual-porosity model and discrete fracture network model. *KSCE Journal of Civil Engineering* 1999; **3**(2):171–180.

DOI: 10.1002/nag

12. Osher S, Sethian JA. Fronts propagating with curvature-dependent speed: algorithms based on Hamilton–Jacobi formulations. *Journal of Computational Physics* 1988; **79**(1):12–49.
13. Duflot M. A study of the representation of cracks with level sets. *International Journal for Numerical Methods in Engineering* 2007; **70**(11):1261–1302.
14. Ghafouri HR, Lewis RW. A finite element double porosity model for heterogeneous deformable porous media. *International Journal for Numerical And Analytical Methods in Geomechanics* 1996; **20**(11):831–844.
15. Lewis RW, Ghafouri HR. A novel finite element double porosity model for multiphase flow through deformable fractured porous media. *International Journal for Numerical And Analytical Methods in Geomechanics* 1997; **21**(11):789–816.
16. Al-Khoury R, Sluys LJ. A computational model for fracturing porous media. *International Journal for Numerical Methods in Engineering* 2006; **70**:423–444.
17. de Borst R, Réthoré J, Abellan M-A. A numerical approach for arbitrary cracks in a fluid-saturated medium. *Archive of Applied Mechanics* 2006; **75**(10):595–606.
18. Réthoré J, Borst R, Abellan M-A. A discrete model for the dynamic propagation of shear bands in a fluid-saturated medium. *International Journal for Numerical And Analytical Methods in Geomechanics* 2007; **31**(2):347–370.
19. Daux C, Moes N, Dolbow J, Sukumar N, Belytschko T. Arbitrary branched and intersecting cracks with the extended finite element method. *International Journal for Numerical Methods in Engineering* 2000; **48**(12):1741–1760.
20. Dolbow J. An extended finite element method with discontinuous enrichment for applied mechanics. In *Department of Theoretical and Applied Mechanics*. Northwestern University: Evanston, IL, USA, 1999.
21. Moës N, Dolbow J, Belytschko T. A finite element method for crack growth without remeshing. *International Journal for Numerical Methods in Engineering* 1999; **46**(1):131–150.
22. Budyn E, Zi G, Moës N, Belytschko T. A method for multiple crack growth in brittle materials without remeshing. *International Journal for Numerical Methods in Engineering* 2004; **61**:1741–1770.
23. Moës N, Gravouil A, Belytschko T. Non-planar 3D crack growth by the extended finite element and level sets – part ι: mechanical model. *International Journal for Numerical Methods in Engineering* 2002; **53**:2549–2568.
24. Stolarska M, Chopp DL, Moës N, Belytschko T. Modelling crack growth by level sets in the extended finite element method. *International Journal for Numerical Methods in Engineering* 2001; **51**(8):943–960.
25. Sukumar N, Moës N, Moran B, Belytschko T. Extended finite element method for three-dimensional crack modelling. *International Journal for Numerical Methods in Engineering* 2000; **48**:1549–1570.
26. Bordas S, Rabczuk T, Zi G. Three-dimensional crack initiation, propagation, branching and junction in non-linear materials by an extended meshfree method without asymptotic enrichment. *Engineering Fracture Mechanics* 2008; **75**(5):943–960.
27. Huang R, Sukumar N, Prévost JH. Modeling quasi-static crack growth with the extended finite element method part ii: numerical applications. *International Journal of Solids and Structures* 2003; **40**(26):7539–7552.
28. Gravouil A, Moës N, Belytschko T. Non-planar 3D crack growth by the extended finite element and level sets—part ii: level set update. *International Journal for Numerical Methods in Engineering* 2002; **53**(11):2569–2586.
29. Lewis RW, Shrefler BA. *The finite element method in the static and dynamic deformation and consolidation of porous media* (2nd). John Wiley: Chichester; New York, 1998; xiii, 492.
30. Schrefler BA, Simoni L. Non-isothermal consolidation of unbounded porous media using mapped infinite elements. *Communications in Applied Numerical Methods* 1987; **3**(5):445–452.
31. Simoni L, Schrefler BA. Mapped infinite elements in soil consolidation. *International Journal for Numerical Methods in Engineering* 1987; **24**(3):513–527.
32. Witherspoon PA, Wang JSY, Iwai K, Gale JE. Validity of cubic law for fluid flow in a deformable rock fracture. *Water Resources Research* 1980; **16**(6):1016–1024.
33. Prabel B, Combescure A, Gravouil A, Marie S. Level set X-FEM non-matching meshes: application to dynamic crack propagation in elastic-plastic media. *International Journal for Numerical Methods in Engineering* 2007; **69**(8):1553–1569.
34. Stazi FL, Budyn E, Chessa J, Belytschko T. An extended finite element method with higher-order elements for curved cracks. *Computational Mechanics* 2003; **31**(1-2):38–48.
35. Sukumar N, Chopp DL, Moës N, Belytschko T. Modeling holes and inclusions by level sets in the extended finite-element method. *Computer Methods in Applied Mechanics and Engineering* 2001; **190**(46-47):6183–6200.
36. Ventura G, Budyn E, Belytschko T. Vector level sets for description of propagating cracks in finite elements. *International Journal for Numerical Methods in Engineering* 2003; **58**(10):1571–1592.
37. Belytschko T, Black T. Elastic crack growth in finite elements with minimal remeshing. *International Journal for Numerical Methods in Engineering* 1999; **45**(5):601–620.
38. Fleming M, Chu YA, Moran B, Belytschko T. Enriched element-free galerkin methods for crack tip fields. *International Journal for Numerical Methods in Engineering* 1997; **40**(8):1483–1504.
39. Bechet E, Minnebol H, Moes N, Burgardt B. Improved implementation and robustness study of the X-FEM for stress analysis around cracks. *International Journal for Numerical Methods in Engineering* 2005; **64**(8):1033–1056.
40. Laborde P, Pommier J, Renard Y, Salaun M. High-order extended finite element method for cracked domains. *International Journal for Numerical Methods in Engineering* 2005; **64**(3):354–381.
41. Belytschko T, Gracie R, Ventura G. A review of extended/generalised finite element methods for mechanics. *Modelling and Simulation in Materials Science and Engineering* 2009; **17**(4):043001.
42. McTigue DF. Thermoelastic response of fluid-saturated porous rock. *Journal of Geophysical Research* 1986; **91**(B9):9533–9542.

DOI: 10.1002/nag

43. Sukumar N, Prévost JH. Modeling quasi-static crack growth with the extended finite element method part i: computer implementation. *International Journal of Solids and Structures* 2003; **40**(26):7513–7537.
44. Babuška I. Error-bounds for finite element method. *Numerische Mathematik* 1971; **16**(4):322–333.
45. Babuška I. The finite element method with lagrangian multipliers. *Numerische Mathematik* 1973; **20**(3):179–192.
46. Brezzi F. Existence, uniqueness and approximation of saddle-point problems arising from lagrangian multipliers. *Revue Francaise D Automatique Informatique Recherche Operationnelle* 1974; **8**(NR2):129–151.
47. Mandel J. Consolidation des sols (étude mathématique). *Geotechnique* 1953; **3**(7):287–299.
48. Cryer CW. A comparison of the three-dimensional consolidation theories of Biot and Terzaghi. *The Quarterly Journal of Mechanics and Applied Mathematics* 1963; **16**(4):401–412.
49. Hughes TJR. *The finite element method : Linear static and dynamic finite element analysis*. Dover Publications: Mineola, NY, 2000; 682.
50. Fish J, Belytschko T. *A first course in finite elements*. John Wiley & Sons Ltd.: Chichester, England; Hoboken, NJ, 2007; xiv; 319.

DOI: 10.1002/nag